

$\mathcal{N} = 4$ chiral superconductivity in moiré transition metal dichalcogenides

Michael M. Scherer,¹ Dante M. Kennes,^{2,3} and Laura Classen⁴

¹*Institut für Theoretische Physik, Universität zu Köln, 50937 Cologne, Germany*

²*Institute for Theory of Statistical Physics, RWTH Aachen University,
and JARA Fundamentals of Future Information Technology, 52056 Aachen, Germany*

³*Max Planck Institute for the Structure and Dynamics of Matter,
Center for Free Electron Laser Science, Luruper Chaussee 149, 22761 Hamburg, Germany*

⁴*Condensed Matter Physics & Materials Science Division,
Brookhaven National Laboratory, Upton, NY 11973-5000, USA*

Experimental demonstrations of tunable correlation effects in magic-angle twisted bilayer graphene [1–7] have put two-dimensional moiré quantum materials at the forefront of condensed-matter research [8]. Other twisted few-layer graphitic structures [9–16], boron-nitride [17], and homo- or hetero-stacks of transition metal dichalcogenides (TMDs) [18–24] have further enriched the opportunities for analysis and utilization of correlations in these systems. Recently, within the latter material class, strong spin-orbit coupling [23, 24] or excitonic physics [25–27] were experimentally explored. The observation of a Mott insulating state [28, 29] and other fascinating collective phenomena such as generalized Wigner crystals [29], stripe phases [30] and quantum anomalous Hall insulators [31] confirmed the relevance of many-body interactions, and demonstrated the importance of their extended range. Since the interaction, its range, and the filling can be tuned experimentally by twist angle, substrate engineering and gating, we here explore Fermi surface instabilities and resulting phases of matter of hetero-bilayer TMDs. Using an unbiased renormalization group approach, we establish in particular that hetero-bilayer TMDs are unique platforms to realize topological superconductivity with winding number $|\mathcal{N}| = 4$. We show that this state reflects in pronounced experimental signatures, such as distinct quantum Hall features.

The pairing of electrons in a superconductor is among the most intriguing effects in the study of collective phenomena. In the quest to achieve ever higher critical temperatures unconventional superconducting states have received an increasing amount of attention [32, 33] as they allow superconducting temperatures beyond the bounds of standard BCS theory [34]. At the same time, combining superconductivity with non-trivial topology is a promising route for quantum information sciences as such topological superconductors may harbor robust edge states at domain boundaries with topological properties advantageous to computing applications [35].

However, realizing and controlling topological superconductors proves difficult to this date, with only a few candidate materials currently being suggested, e.g., [36–40]. A new direction in the study of superconductivity

opened up recently in twisted moiré quantum materials, i.e. two-dimensional van der Waals materials being stacked at a relative twist angle [1–17, 41, 42]. In these systems kinetic energy scales can be tuned by the twist angle allowing to promote the relative relevance of potential, spin-orbit coupling or other energy scales [8]. Indeed, topological properties as well as superconductivity were already demonstrated in these highly versatile systems and as a consequence they could provide an excellent opportunity to engineer novel topological superconductors.

Here, we explore this idea for moiré transition metal dichalcogenides (see Fig. 1a) [8, 18–24, 28] by analyzing the Fermi surface instabilities of twisted hetero-bilayers of WX_2/MoX_2 ($\text{X}=\text{S},\text{Se}$) away from half filling of the moiré band. We unveil an exotic superconducting state near Van Hove filling described by form factors with eight zero crossings, arising from the extended range of interactions in these materials. We show that the superconducting ground state is formed by a chiral configuration, which is characterized by a full gap on the Fermi surface and non-trivial topology with winding number $|\mathcal{N}| = 4$. We argue that this type of topological superconductivity leads to distinct experimental signatures in quantum Hall transport measurements and elevates twisted hetero-bilayers of TMDs to prime candidates for experimental scrutiny of topological superconductivity.

In a range of small twist angles, isolated and narrow moiré bands emerge in TMD hetero-bilayers of WX_2/MoX_2 ($\text{X}=\text{S},\text{Se}$) [18–24]. These flat bands are formed by the highest, spin-polarized valence band of WX_2 and can be described by an extended triangular-lattice Hubbard model $H = H_0 + H_I$, which features an effective $\text{SU}(2)$ valley symmetry [18]

$$H_0 = \sum_{v=\pm} \left[\sum_{ij} t_{i-j} c_{i,v}^\dagger c_{j,v} - \mu \sum_i c_{i,v}^\dagger c_{i,v} \right] \quad (1)$$

$$H_I = U \sum_i n_{i,+} n_{i,-} + \sum_{ij} V_{i-j} n_i n_j. \quad (2)$$

Here, $n_i = \sum_v n_{i,v}$ and $n_{i,v} = c_{i,v}^\dagger c_{i,v}$ is the number of electrons on site i with valley index \pm , $c_{i,v}^{(\dagger)}$ are the corresponding annihilation (creation) operators. The hopping amplitudes t_n for the n th-nearest neighbors depend on the twist angle and we consider typical values for vanish-

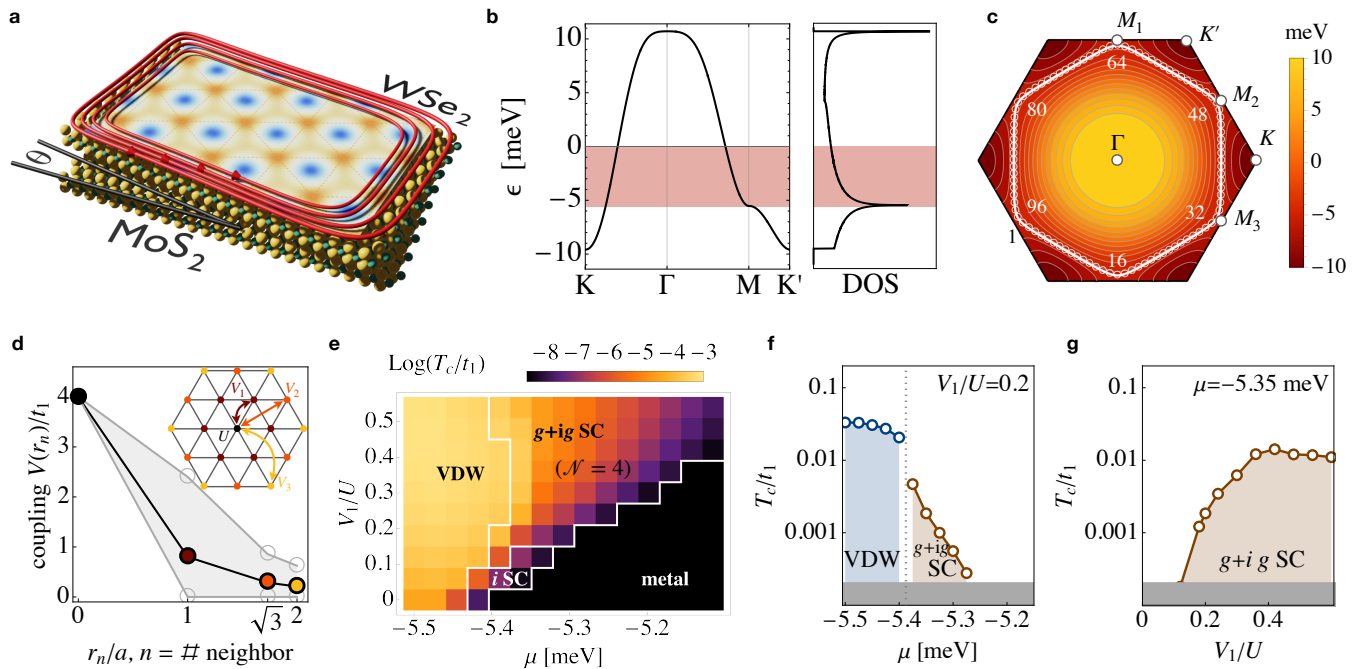


FIG. 1. **Correlated phase diagram of hetero-bilayer TMDs.** **a** Sketch of a twisted $\text{WSe}_2/\text{MoS}_2$ bilayer with small twist angle θ . The resulting effective moiré potential [18, 24] is indicated by the contour shading at the top. The four red lines represent the chiral edge modes of the topological superconducting state with $\mathcal{N} = 4$. **b** Dispersion of the energy band $\epsilon_{\vec{k}}$ along high-symmetry lines and density of states (DOS). We explore filling levels indicated by the red band between half filling ($\mu \sim 0$) and Van Hove filling ($\mu = -5.5\text{meV}$, $\sim 1/4$ filling). **c** Nearly nested Fermi surface close to the Van Hove energy. Numbered open circles show the momentum resolution of the Fermi surface employed in the FRG approach. **d** Extended interaction parameters as function of distance r_n/a , a is the moiré lattice spacing [18, 24]. The gray area marks the explored range of interactions, which are tunable by the environment. Inset: sketch of the interactions on the triangular moiré lattice. **e** Phase diagram as function of nearest-neighbor repulsion V_1 and filling controlled by the chemical potential μ extracted from the Fermi-liquid instabilities in the FRG flow for $U = 4t_1$, $V_2/V_1 = 0.357$ and $V_3/V_1 = 0.260$ (see Fig. 1d). The background color encodes our estimate for the critical temperature (see methods). We find an instability towards a valley density wave (VDW) near Van Hove filling $\mu \approx -5.5\text{meV}$. It is flanked by an i -wave superconducting instability (i SC) for small V_1/U and by a g -wave superconducting instability for larger V_1/U . In the ground state, the g -wave superconducting instability forms a chiral $g + ig$ state ($g + ig$ SC) characterized by winding number $\mathcal{N} = 4$. The regime colored in black, does not show any instability within our numerical accuracy. **f** Filling-dependent critical temperature near Van Hove filling. Below the gray band, we cannot resolve any instability within our numerical accuracy. **g** Dependence of the critical temperature on the extended interactions tuned via V_1/U at fixed $V_2/V_1, V_3/V_1$ slightly away from Van Hove filling.

ingly small twist angle $t_1 \approx 2.5\text{meV}$, $t_2 \approx -0.5\text{meV}$, $t_3 \approx -0.25\text{meV}$ [18]. The resulting moiré band $\epsilon_{\vec{k}}$ features a Van Hove peak in the density of states near $1/4$ filling (-5.5meV), where the Fermi surface is approximately nested (Fig. 1b,c). In experiment, the filling can be adjusted, and Van Hove filling can be reached, by tuning the gate voltage, which we model here by varying the chemical potential μ between $1/4$ and $1/2$ filling. The interaction parameters U, V_n also depend on the twist angle, and on the dielectric environment so that the strength and range of interactions can be controlled [43]. First-principles calculations show that the extended interactions V_n are sizable in effective models for hetero-bilayer TMDs [18]. For our analysis, we use an intermediate interaction strength for the onsite interaction $U = 4t_1$ and explore the effect of further-ranged interactions by varying $V_1/U \in [0, 0.5]$ with $V_2/V_1 \approx 0.357$

and $V_3/V_1 \approx 0.260$ [18, 24] (Fig. 1d). In a second step we also investigate the impact of an additional nearest-neighbor exchange interaction $H_J = J \sum_{\langle i,j \rangle} \vec{S}_i \vec{S}_j$ to model strong-coupling effects.

We study the correlated phases of hetero-bilayer TMDs that emerge out of a metallic state within an itinerant scenario using the fermionic functional renormalization group (FRG) [44]. The FRG resolves the competition between different ordering tendencies in an unbiased way and is employed to calculate the dressed, irreducible two-particle correlation function $V(\vec{k}_1, \vec{k}_2, \vec{k}_3, \vec{k}_4)$ for electrons with momenta \vec{k}_i , $i = 1 \dots 4$, on the Fermi surface (Fig. 1c). Upon lowering the temperature, $V(\vec{k}_1, \vec{k}_2, \vec{k}_3, \vec{k}_4)$ develops sharp, localized peaks for characteristic momentum combinations, indicating long-ranged correlations in real space. This allows us to ex-

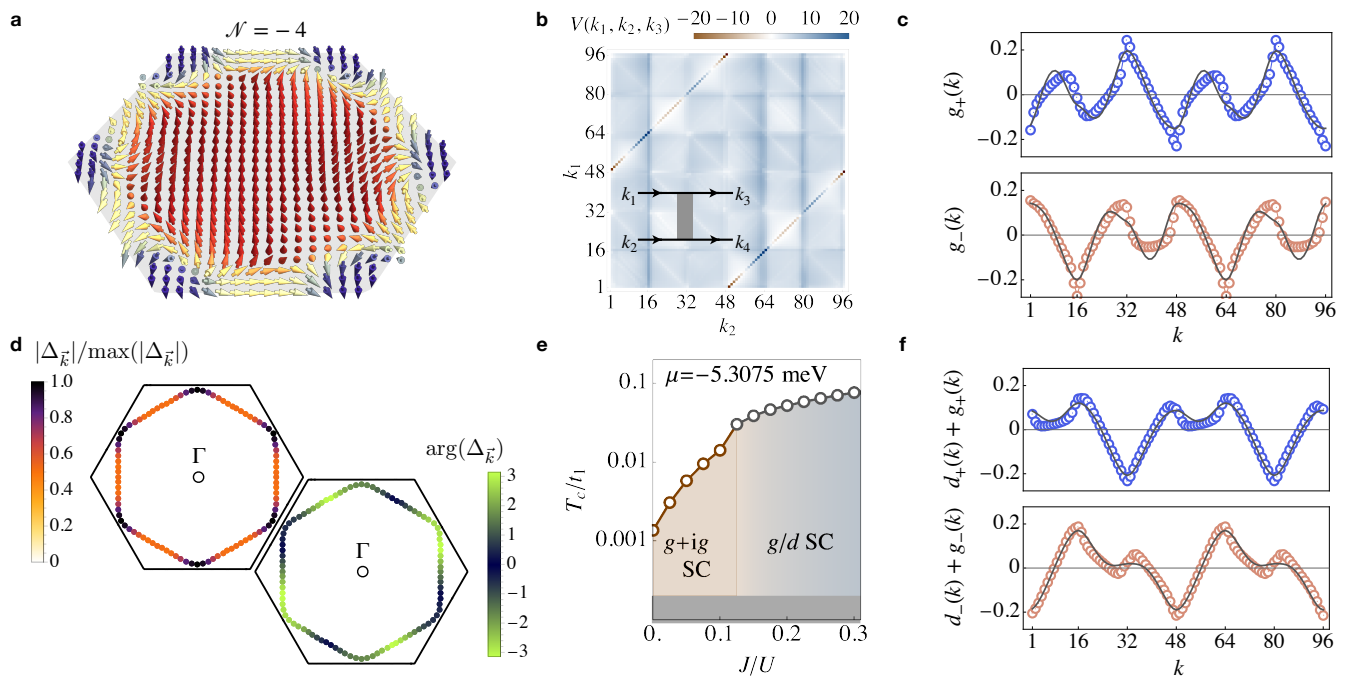


FIG. 2. Topological superconductivity in hetero-bilayer TMDs. **a** The phase winding of the superconducting gap in the $g + ig$ state can be visualized by a skyrmion configuration constructed from the vector $\vec{m} = (\text{Re}\Delta_{\vec{k}}, \text{Im}\Delta_{\vec{k}}, \xi_{\vec{k}})/(\xi_{\vec{k}}^2 + |\Delta_{\vec{k}}|^2)^{1/2}$. \vec{m} points up (down) at the highest (lowest) energies $\xi_{\vec{k}} = \epsilon_{\vec{k}} - \mu$ and rotates \mathcal{N} times in the plane in the vicinity of the Fermi level $\xi_{\vec{k}} = 0$. The skyrmion configuration is used to calculate the winding number \mathcal{N} , which for a broad range of fillings around Van Hove filling is $|\mathcal{N}| = 4$, indicating an enhanced response in thermal and spin quantum Hall measurements. **b** Functional RG data of the irreducible two-particle correlation function $V(\vec{k}_1, \vec{k}_2, \vec{k}_3, \vec{k}_4)$ near the instability temperature for incoming wave vectors \vec{k}_1, \vec{k}_2 . Wave vectors are labeled by the patch points along the Fermi surface indicated in Fig. 1c. The outgoing wave vector \vec{k}_3 is fixed at patch no. 1 and $\vec{k}_4 = \vec{k}_1 + \vec{k}_2 - \vec{k}_3$ is given by momentum conservation. The sharp diagonal features occur at $\vec{k}_1 = -\vec{k}_2, \vec{k}_3 = -\vec{k}_4$, indicating the formation of long-ranged superconducting correlations. **c** Superconducting form factors $g_{\pm}(k)$ extracted from $V(\vec{k}_1, \vec{k}_2, \vec{k}_3, \vec{k}_4)$ in b. They exhibit a large overlap with a linear combination of the second-nearest-neighbor lattice harmonics $g_1(\vec{k}), g_2(\vec{k})$ (solid gray lines) defined in the text, which belong to the two-dimensional irreducible representation E_2 of the lattice symmetry group C_{6v} . We classify them as g -wave form factors due to their eight nodes. **d** Absolute value and phase of the gap function on the Fermi surface. The chiral superposition $\Delta_{\vec{k}} = |\Delta|[(g_1(\vec{k}) \pm ig_2(\vec{k}))]$ fully gaps the Fermi surface, thereby minimizing the energy. Such a $g + ig$ superconducting state breaks time-reversal symmetry and is topological with a four-fold phase winding along the Fermi surface $|\mathcal{N}| = 4$. **e** Stability of the g -wave superconducting state towards inclusion of J/U for $V_1/U = 0.2$ at $\mu = 5.3075$ meV. For growing values of the exchange interaction J , the nearest-neighbor harmonics d_1 and d_2 of E_2 (defined in the text) start to contribute as indicated by the colored transition. They are pure d -wave form factors with only four nodes. For $J/U \lesssim 0.1$, the contribution from d_1 and d_2 is negligible. **f** Example of the extracted form factors for $J/U = 0.5$ where d_1, d_2 and g_1, g_2 roughly contribute by equal amounts, showing the change in the number of nodes due to the admixture.

tract the temperature where a strongly-correlated state forms, as well as the symmetry and type of the strongest correlations (see methods).

In our model for hetero-bilayer TMD moiré systems, instabilities near $1/4$ filling occur due to the high density of states and approximate nesting, which leads to symmetry-broken ground states. We start with varying μ and V_n and calculate the phase diagram based on the two-particle correlation functions (Fig. 1e). Closest to Van Hove filling $\mu \approx -5.5$ meV, we find that correlations corresponding to a valley density wave (VDW) are strongest, which manifest themselves by peaks at the nesting momenta \vec{Q}_{α} , $\alpha = 1, 2, 3$ in $V(\vec{k}_1, \vec{k}_2, \vec{k}_3, \vec{k}_4)$,

i.e. at $k_3 - k_1 = Q_{\alpha}$ or $k_3 - k_2 = Q_{\alpha}$. This state is the analogue of a spin density wave [45, 46] considering that, here, the $SU(2)$ symmetry belongs to a pseudo-spin formed by the valleys. The VDW instability is insensitive towards the inclusion of V_n in the explored range.

Moving the filling slightly away from Van Hove filling, we obtain a superconducting instability, which is indicated by diagonal peak positions, i.e. $V(\vec{k}_1, \vec{k}_2, \vec{k}_3, \vec{k}_4) \approx V(k_1, -k_1, k_3, -k_3)$, that correspond to electron pairs with a total momentum of zero $k_1 + k_2 = k_3 + k_4 = 0$ (Fig. 2b). Increasing the filling further reduces the critical temperature until it vanishes (Fig. 1f). The inclusion of V_n has a profound impact: it strongly affects the

symmetry of the superconducting correlations, because it penalizes electrons to be simultaneously on neighboring sites, so that electron pairing is shifted to farther-distanced neighbors. As a result, the largest attraction is promoted to occur in a higher-harmonic channel.

The symmetry of the pair correlations can be classified in terms of the irreducible representations of the lattice point group C_{6v} by expanding the eigenfunctions of $V(\vec{k}, -\vec{k}, \vec{k}', -\vec{k}')$ in lattice harmonics. Within an irreducible representation, lattice harmonics with the same symmetry but different angular-momentum form factors can mix and it depends on microscopic details which lattice harmonics are the strongest.

For small V_n , we find a small regime with A_2 symmetry (i -wave) in agreement with previous results for $V_n = 0$ [47, 48]. However, for larger V_n ($V_1/U \gtrsim 0.15$), including realistic values in twisted TMDs [18, 24], we unveil a large regime with a different symmetry. That V_1 drives this instability can also be seen at the critical temperature, which initially increases with V_1 and then saturates (see Fig. 1g). The pair correlations in this regime are fitted well using the second-nearest-neighbor lattice harmonics $g_1(\vec{k}) = 8/9[-\cos(3k_x/2)\cos(\sqrt{3}k_y/2) + \cos(\sqrt{3}k_y)]$, $g_2(\vec{k}) = 8/(3\sqrt{3})\sin(3k_x/2)\sin(\sqrt{3}k_y/2)$ (Fig. 2c). They belong to the two-dimensional irreducible representation E_2 , which contains both, d - and g -wave form factors. While they cannot, in principle, be distinguished by symmetry, we can categorize our result as g -wave based on the number of nodes [49]. This has unique, measurable consequences for the topological properties of the superconducting state.

Due to the two-dimensional E_2 symmetry, the superconducting gap has two components Δ_1, Δ_2 and additional symmetries besides $U(1)$ can be broken depending on the configuration that forms the ground state [50]. The ground-state configuration is determined by minimizing the Landau energy functional

$$\mathcal{L} = \alpha(|\Delta_1|^2 + |\Delta_2|^2) + \beta(|\Delta_1|^2 + |\Delta_2|^2)^2 + \gamma|\Delta_1^2 + \Delta_2^2|. \quad (3)$$

We use our FRG results as an input for the effective interaction $V(\vec{k}, -\vec{k}, \vec{k}', -\vec{k}')c_{\vec{k}',v}^\dagger c_{-\vec{k}',v}^\dagger c_{-\vec{k},v} c_{\vec{k},v}$ close to the instability and perform a Hubbard-Stratonovich decoupling with the pairing fields $\Delta_i \sim g_i(\vec{k})c_{\vec{k},+} c_{-\vec{k},-}$, $\Delta_i^* \sim g_i(\vec{k})c_{-\vec{k},-}^\dagger c_{\vec{k},+}^\dagger$. Integrating out the electrons, we find in particular $\gamma > 0$. Thus, the chiral configuration $\Delta_1 = i\Delta_2$ minimizes the energy. Such a “ $g + ig$ ” superconducting state breaks time-reversal symmetry and is topologically non-trivial. The Fermi surface is fully gapped as we can see from the quasiparticle energy $E_{\vec{k}} = (\xi_{\vec{k}}^2 + |\Delta_{\vec{k}}|^2)^{1/2}$, where $\xi_{\vec{k}} = \epsilon_{\vec{k}} - \mu$, $\Delta_{\vec{k}} = \Delta[g_1(\vec{k}) + ig_2(\vec{k})]$, and g_1, g_2 are the FRG-extracted form factors (see Figs. 2c,d). The topological properties can be classified by an integer invariant based on the

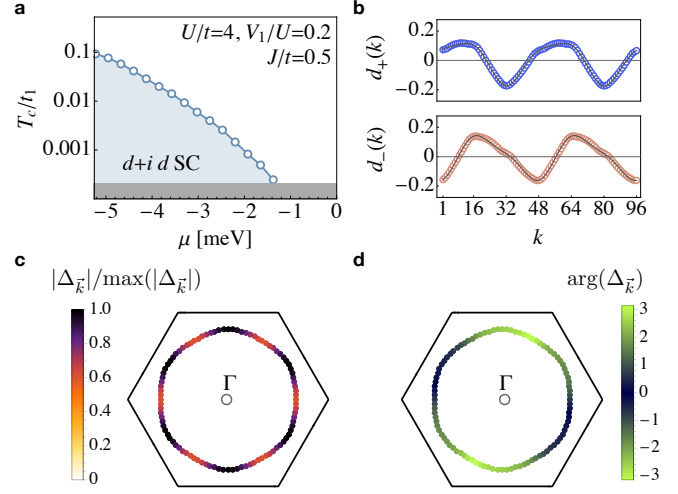


FIG. 3. **Effect of exchange coupling.** **a** Filling-dependent critical temperature for a sizable exchange coupling $J/t = 0.5$. The exchange coupling generates a d -wave instability, which indicates a chiral $d+id$ ground state. **b** Superconducting form factors $d_{\pm}(k)$ extracted from $V(\vec{k}_1, \vec{k}_2, \vec{k}_3, \vec{k}_4)$ which exhibit a large overlap with a linear combination of nearest-neighbor lattice harmonics d_1, d_2 (solid gray lines) defined in the text. Their chiral superposition $d \pm id$ fully gaps the Fermi surface with the gap function $\Delta(k)$ shown in the lowest panels (**c,d**). The phase winds twice around the Fermi surface.

Skyrmion number [51–53]

$$\mathcal{N} = \frac{1}{4\pi} \int_{\text{BZ}} d^2k \vec{m} \cdot \left(\frac{\partial \vec{m}}{\partial k_x} \times \frac{\partial \vec{m}}{\partial k_y} \right), \quad (4)$$

where the pseudo-spin vector is given by $\vec{m} = (\text{Re}\Delta_{\vec{k}}, \text{Im}\Delta_{\vec{k}}, \xi_{\vec{k}})/E_{\vec{k}}$ (Fig. 2a). \vec{m} follows the phase winding of the superconducting gap around the Fermi surface. We calculate \mathcal{N} for the entire range of fillings and find $|\mathcal{N}| = 4$ in the relevant regime where the superconducting instability occurs. Importantly, the high winding number $|\mathcal{N}| = 4$ implies stronger experimental signatures compared to other topological superconductors. Four chiral edge modes appear (as illustrated in Fig. 1a) and the quantized thermal and spin response is enhanced with the spin Hall conductance given by $\sigma_{xy}^s = \mathcal{N}\hbar/(8\pi)$ and the thermal Hall conductance by $\kappa = \mathcal{N}\pi k_B^2/(6\hbar)$ [54, 55].

The $g + ig$ pairing state is robust with respect to the inclusion of small to intermediate nearest-neighbor exchange J . For example, for $V_1/U = 0.2$ and $\mu \approx -5.31$ meV, $g + ig$ pairing is dominant up to reasonably large values of $J \approx 0.1$ (Fig. 2e). For larger values of J , d -wave contributions from the nearest-neighbor form factors $d_1(\vec{k}) = 2(\cos k_x - \cos(k_x/2)\cos(\sqrt{3}k_y/2))$ and $d_2(\vec{k}) = 3/\sqrt{3}\sin(k_x/2)\sin(\sqrt{3}k_y/2)$ start to mix with the previous g -wave ones g_1, g_2 (see Figs. 2e,f). This is expected when the attraction mediated by antiferro-

magnetic fluctuations from J overcomes the repulsion from V_n . For larger values of J and farther away from Van Hove filling, the d -wave form factors dominate (see Figs. 3a,b). Then, the superconducting ground state is a fully gapped $d+id$ state with $|\mathcal{N}| = 2$, which can be seen from the phase of the superconducting state winding two times along the Fermi surface (see Figs. 3c,d).

Our results highlight twisted hetero-bilayers of TMDs as prime candidates for exotic topological superconducting states in two-dimensional materials. They allow — by moiré or substrate engineering — for an unprecedented level of external control [8] and our identification of topological $g+ig$ superconductivity opens up pathways to interrogate this elusive phase of matter in a highly tunable setup. Exploiting the unparalleled level of control, these platforms provide the opportunity to scrutinize topological phase transitions using gating which, as we showed, drives the $g+ig$ state into a density wave or a metallic state at either side of the topological superconductor. This can also shed light on related questions about topological transitions, e.g., the nodal structure at the transition point from $|\mathcal{N}| = 2$ to $|\mathcal{N}| = 4$, which is intensely debated for Na_xCoO_2 [56, 57]. An intriguing avenue of future research concerns the relevance of (magnetic as well as non-magnetic) disorder and finite size effects onto the g -wave superconducting state as moiré materials tend to form localized dislocations [58]. From a theoretical angle, the recently developed real-space extension of the unbiased renormalization scheme used here might provide insights into these questions [59]. Another interesting possibility is to investigate if non-local Coulomb interactions can also induce topological triplet superconductivity as discussed for Ref. [60].

Experimentally, the prediction of $g+ig$ topological superconductivity can be verified using thermal or spin quantum Hall measurements which reveals the four-fold nature of the chiral and topologically protected edge modes. Domain walls between $\mathcal{N} = +4$ and -4 configurations must host eight propagating chiral modes [51]. Whether these edge modes can be utilized for future quantum information technologies requires additional investigation [61]. The option appears particularly intriguing with twisted hetero-bilayers of TMDs being so highly tunable and the energy scales on which the material properties can be altered being so low due to the flat bands.

METHODS

We have employed the functional renormalization group method to explore the phase diagram of our model [44, 62, 63]. Within the FRG, we choose the temperature as the flow parameter and use an approximation that neglects feed-back from the self-energy and three-particle vertices or higher. In this approximation, we obtain a renormalization group equation for the two-particle correlation function $\Gamma^{(2p)}$ that describes its evolution upon lowering the temperature.

In an SU(2)-symmetric system, $\Gamma^{(2p)}$ can be expressed via a (pseudo-)spin-independent coupling function V as $\Gamma^{(2p)}_{s_1 s_2 s_3 s_4}(k_1, k_2, k_3, k_4) = V(k_1, k_2, k_3, k_4)\delta_{s_1 s_3}\delta_{s_2 s_4} - V(k_1, k_2, k_4, k_3)\delta_{s_1 s_4}\delta_{s_2 s_3}$, where s_i labels the (pseudo-)spin, and k_1, k_2 are incoming and k_3, k_4 outgoing momenta. Momentum conservation requires $k_1 + k_2 = k_3 + k_4$, so for brevity we will use $V(k_1, k_2, k_3) = V(k_1, k_2, k_3, k_1 + k_2 - k_3)$ in the following.

The RG equation for the temperature evolution of $V(k_1, k_2, k_3)$ can then be written as

$$\frac{d}{dT}V = \tau_{\text{pp}} + \tau_{\text{ph,d}} + \tau_{\text{ph,cr}}. \quad (5)$$

with contributions from the particle-particle, the direct particle-hole, and the crossed particle-hole channel on the right hand side. They are given by

$$\tau_{\text{pp}} = -\frac{1}{2} \int_{\text{BZ}} d^2k V(k_1, k_2, k) L(k, q_{\text{pp}}) V(k, q_{\text{pp}}, k_3),$$

where we used the short hand $\int_{\text{BZ}} d^2k = -A_{\text{BZ}}^{-1} \int d^2k$ and A_{BZ} is the area of the Brillouin zone. The particle-hole contributions read

$$\begin{aligned} \tau_{\text{ph,d}} = \frac{1}{2} \int_{\text{BZ}} d^2k [& 2V(k_1, k, k_3) L(k, q_{\text{d}}) V(q_{\text{d}}, k_2, k) \\ & - V(k, k_1, k_3) L(k, q_{\text{d}}) V(q_{\text{d}}, k_2, k) \\ & - V(k, k_1, k_3) L(k, q_{\text{d}}) V(k_2, q_{\text{d}}, k)], \end{aligned}$$

and

$$\tau_{\text{ph,cr}} = -\frac{1}{2} \int_{\text{BZ}} d^2k V(k, k_2, k_3) L(k, q_{\text{cr}}) V(k_1, q_{\text{cr}}, k).$$

In these expressions, we introduced $q_{\text{pp}} = -k + k_1 + k_2$, $q_{\text{d}} = k + k_1 - k_3$, $q_{\text{cr}} = k + k_2 - k_3$, and the loop kernel

$$L(k, \pm k + k') = \frac{d}{dT} \left[T \sum_{i\omega} G_0(i\omega, k) G_0(\pm i\omega, \pm k + k') \right],$$

with the free propagator $G_0(i\omega, k) = [i\omega - \xi_k]^{-1}$. In these expressions, we have neglected the (external) frequency dependence assuming that the strongest correlations occur for the lowest Matsubara frequencies.

For the numerical implementation, we resolve the momentum dependence in a so-called patching scheme that divides the Fermi surface into N pieces based on equidistant angles and treats the radial dependence for a fixed angle as constant. This accurately describes the relevant momentum dependence, which is along the Fermi surface. In our numerical calculations, we have chosen between $N = 48$ and $N = 96$ patches, cf. Fig. 1b. Our results on the type of instability do not depend on this choice and the quantitative results for critical temperatures vary only mildly with N .

The initial condition for $V(k_1, k_2, k_3)$ at high temperatures is given by the Fourier transform of H_I in Eq. (2). We set $T_0 = \max(\epsilon_k)$ as starting temperature. We then

calculate the temperature evolution of $V(k_1, k_2, k_3)$ according to Eq. (5) by solving the integro-differential equation. As described above, the development of strong correlations is signaled by a diverging $V(k_1, k_2, k_3)$ at a critical temperature T_c . Our numerical criterion to detect the divergence is a convex temperature dependence and $\max[V(k_1, k_2, k_3)]$ exceeding $30t_1$. T_c would be the mean-field critical temperature in an RPA resummation, however, here the estimate is slightly improved due to the inclusion of the coupling between different channels. The Fermi liquid is stable within our numerical accuracy if no divergence occurs before $T_l = 2 \cdot 10^{-4}t_1$ is reached. In the cases when correlated states develop, we can read off the type of correlations from the momentum structure of $V(k_1, k_2, k_3)$ at T_c . Up to an overall constant, this determines the effective interaction close to the instability and directly suggests the order-parameter corresponding to the instability. Following this procedure for an extended range of parameters, we obtain the presented phase diagrams. To extract the form factors of the superconducting instabilities, we diagonalize $V(k, -k, k')$, keep the eigenfunction(s) with the largest eigenvalue and approximate it by lattice harmonics.

We have used the extracted lattice harmonics to derive the Landau functional (3) from our microscopic model. The decisive prefactor of the term $|\Delta_1^2 + \Delta_2^2|^2$ is given by

$$\begin{aligned} \gamma &= T \sum_{i\omega} \int_{\text{BZ}} d^2k \frac{g_1(\vec{k})^2 g_2(\vec{k})^2}{(i\omega - \xi_{\vec{k}})^2 (i\omega + \xi_{\vec{k}})^2} \\ &= \int_{\text{BZ}} d^2k g_1(\vec{k})^2 g_2(\vec{k})^2 \frac{1 - 2n_F(\xi_{\vec{k}}) + 2\xi_{\vec{k}} n'_F(\xi_{\vec{k}})}{4\xi_{\vec{k}}^3} \quad (6) \end{aligned}$$

with the Fermi function n_F . We have calculated γ numerically and found it to be positive in the considered range of μ and T . As an analytical estimate for γ , we can approximate the dispersion by $\xi \approx k^2/(2m) - \mu$ with

density of states ρ_ϵ , and the form factors by $g_1 = \cos(n\varphi)$, $g_2 = \sin(n\varphi)$ with $\varphi = \arctan k_y/k_x$ and $n = 4$ for $g + ig$ superconductivity ($n = 2$ for $d + id$ and $n = 1$ for $p + ip$). With this simplification, we obtain

$$\begin{aligned} \gamma &\approx \int d\varphi \cos^2(n\varphi) \sin^2(n\varphi) \int d\epsilon \rho_\epsilon \frac{\frac{1}{2} - n_F(\epsilon) + \epsilon n'_F(\epsilon)}{2\epsilon^3} \\ &= \frac{m}{16\pi T^2} \int \frac{\sinh(x) - x}{4x^3(1 + \cosh(x))} \approx 0.05 \frac{m}{16\pi T^2}, \quad (7) \end{aligned}$$

which we can take as a rough estimate for γ if μ is away from the Van Hove energy. Right at the Van Hove energy, an additional logarithmic dependence on T_c emerges.

Acknowledgements. — We thank Andrey Chubukov and Abhay Pasupathy for useful discussions. MMS acknowledges support by the DFG through SFB 1238 (project C02, project id 277146847). DMK acknowledges support from the Deutsche Forschungsgemeinschaft (DFG, German Research Foundation) through RTG 1995, within the Priority Program SPP 2244 “2DMP”, under Germany’s Excellence Strategy-Cluster of Excellence Matter and Light for Quantum Computing (ML4Q) EXC2004/1 - 390534769, and from the Max Planck-New York City Center for Non-Equilibrium Quantum Phenomena. LC was supported by the U.S. Department of Energy (DOE), Office of Basic Energy Sciences, under Contract No. DE-SC0012704.

Author Contributions. — The work was conceived by LC and MMS. MMS computed functional RG data. All authors analyzed and interpreted the results and wrote the manuscript.

Competing Interests. — The authors declare no competing interests.

Data availability. — Data and simulation codes are available from the corresponding authors upon reasonable request.

-
- [1] Cao, Y. *et al.* Unconventional superconductivity in magic-angle graphene superlattices. *Nature* **556**, 43–50 (2018). URL <http://dx.doi.org/10.1038/nature26160>.
- [2] Cao, Y. *et al.* Correlated insulator behaviour at half-filling in magic-angle graphene superlattices. *Nature* **556**, 80–84 (2018). URL <http://dx.doi.org/10.1038/nature26154>.
- [3] Yankowitz, M. *et al.* Tuning superconductivity in twisted bilayer graphene. *Science* **363**, 1059–1064 (2019). URL <http://dx.doi.org/10.1126/science.aav1910>.
- [4] Kerelsky, A. *et al.* Maximized electron interactions at the magic angle in twisted bilayer graphene. *Nature* **572**, 95–100 (2019). URL <https://doi.org/10.1038/s41586-019-1431-9>.
- [5] Sharpe, A. L. *et al.* Emergent ferromagnetism near three-quarters filling in twisted bilayer graphene. *Science* **365**, 605–608 (2019). URL <https://doi.org/10.1126/science.aaw3780>.
- [6] Lu, X. *et al.* Superconductors, orbital magnets and correlated states in magic-angle bilayer graphene. *Nature* **574**, 20–23 (2019). URL <http://dx.doi.org/10.1038/s41586-019-1695-0>.
- [7] Serlin, M. *et al.* Intrinsic quantized anomalous Hall effect in a moiré heterostructure. *Science* **367**, 900–903 (2020). URL <http://dx.doi.org/10.1126/science.aay5533>.
- [8] Kennes, D. M. *et al.* Moiré heterostructures as a condensed-matter quantum simulator. *Nature Physics* **17**, 155–163 (2021). URL <https://doi.org/10.1038/s41567-020-01154-3>.
- [9] Liu, X. *et al.* Tunable spin-polarized correlated states in twisted double bilayer graphene. *Nature* **583**, 221–225 (2020). URL <https://doi.org/10.1038/s41586-020-2458-7>.
- [10] Cao, Y. *et al.* Tunable correlated states and spin-polarized phases in twisted bilayer–bilayer graphene. *Nature* **583**, 215–220 (2020). URL <https://doi.org/10.1038/s41586-020-2260-6>.

- [11] Shen, C. *et al.* Correlated states in twisted double bilayer graphene. *Nature Physics* **16**, 520–525 (2020). URL <https://doi.org/10.1038/s41567-020-0825-9>.
- [12] Chen, G. *et al.* Evidence of a gate-tunable Mott insulator in a trilayer graphene moiré superlattice. *Nature Physics* **15**, 237–241 (2019). URL <http://dx.doi.org/10.1038/s41567-018-0387-2>.
- [13] Chen, G. *et al.* Signatures of tunable superconductivity in a trilayer graphene moiré superlattice. *Nature* **572**, 215–219 (2019). URL <https://doi.org/10.1038/s41586-019-1393-y>.
- [14] Chen, G. *et al.* Tunable correlated chern insulator and ferromagnetism in a moiré superlattice. *Nature* **579**, 56–61 (2020). URL <https://doi.org/10.1038/s41586-020-2049-7>.
- [15] Burg, G. W. *et al.* Correlated insulating states in twisted double bilayer graphene. *Phys. Rev. Lett.* **123**, 197702 (2019). URL <https://link.aps.org/doi/10.1103/PhysRevLett.123.197702>.
- [16] Rubio-Verdú, C. *et al.* Universal moiré nematic phase in twisted graphitic systems. *arXiv:2009.11645* (2020). URL <https://arxiv.org/abs/2009.11645>.
- [17] Xian, L., Kennes, D. M., Tancogne-Dejean, N., Altarelli, M. & Rubio, A. Multiflat bands and strong correlations in twisted bilayer boron nitride: Doping-induced correlated insulator and superconductor. *Nano Letters* **19**, 4934–4940 (2019). URL <https://doi.org/10.1021/acs.nanolett.9b00986>.
- [18] Wu, F., Lovorn, T., Tutuc, E. & Macdonald, A. H. Hubbard Model Physics in Transition Metal Dichalcogenide Moiré Bands. *Phys. Rev. Lett.* **121**, 26402 (2018). URL <https://doi.org/10.1103/PhysRevLett.121.026402>.
- [19] Wu, F., Lovorn, T., Tutuc, E., Martin, I. & Macdonald, A. H. Topological Insulators in Twisted Transition Metal Dichalcogenide Homobilayers. *Phys. Rev. Lett.* **122**, 86402 (2019). URL <https://doi.org/10.1103/PhysRevLett.122.086402>.
- [20] Naik, M. H. & Jain, M. Ultraflatbands and Shear Solitons in Moiré Patterns of Twisted Bilayer Transition Metal Dichalcogenides. *Phys. Rev. Lett.* **121**, 266401 (2018). URL <https://doi.org/10.1103/PhysRevLett.121.266401>.
- [21] Ruiz-Tijerina, D. A. & Fal'Ko, V. I. Interlayer hybridization and moiré superlattice minibands for electrons and excitons in heterobilayers of transition-metal dichalcogenides. *Phys. Rev. B* **99**, 30–32 (2019). URL <https://link.aps.org/doi/10.1103/PhysRevB.99.125424>.
- [22] Schrade, C. & Fu, L. Spin-valley density wave in moiré materials. *Phys. Rev. B* **100**, 035413 (2019). URL <https://link.aps.org/doi/10.1103/PhysRevB.100.035413>.
- [23] Wang, L. *et al.* Correlated electronic phases in twisted bilayer transition metal dichalcogenides. *Nature Materials* **19**, 861–866 (2020). URL <https://doi.org/10.1038/s41563-020-0708-6>.
- [24] Zhou, Y., Sheng, D. & Kim, E.-A. Quantum phases of transition metal dichalcogenide moiré systems. *arXiv:2105.07008* (2021). URL <https://arxiv.org/abs/2105.07008>.
- [25] Jin, C. *et al.* Observation of moiré excitons in WSe₂/WS₂ heterostructure superlattices. *Nature* **567**, 76–80 (2019). URL <https://doi.org/10.1038/s41586-019-0976-y>.
- [26] Wang, Z. *et al.* Evidence of high-temperature exciton condensation in two-dimensional atomic double layers. *Nature* **574**, 76–80 (2019). URL <https://doi.org/10.1038/s41586-019-1591-7>.
- [27] Shimazaki, Y. *et al.* Strongly correlated electrons and hybrid excitons in a moiré heterostructure. *Nature* **580**, 472–477 (2020). URL <https://doi.org/10.1038/s41586-020-2191-2>.
- [28] Tang, Y. *et al.* WSe₂/WS₂ moiré superlattices: a new Hubbard model simulator. *arXiv:1910.08673* (2019). URL <https://arxiv.org/abs/1910.08673>.
- [29] Regan, E. C. *et al.* Mott and generalized Wigner crystal states in WSe₂/WS₂ moiré superlattices. *Nature* **579**, 359–363 (2020). URL <https://doi.org/10.1038/s41586-020-2092-4>.
- [30] Jin, C. *et al.* Stripe phases in WSe₂/WS₂ moiré superlattices. *Nature Materials* **20**, 940–944 (2021). URL <https://doi.org/10.1038/s41563-021-00959-8>.
- [31] Li, T. *et al.* Quantum anomalous Hall effect from intertwined moiré bands. *arXiv:2107.01796* (2021). URL <https://arxiv.org/abs/2107.01796>.
- [32] Damascelli, A., Hussain, Z. & Shen, Z.-X. Angle-resolved photoemission studies of the cuprate superconductors. *Rev. Mod. Phys.* **75**, 473–541 (2003). URL <https://link.aps.org/doi/10.1103/RevModPhys.75.473>.
- [33] Fischer, O., Kugler, M., Maggio-Aprile, I., Berthod, C. & Renner, C. Scanning tunneling spectroscopy of high-temperature superconductors. *Rev. Mod. Phys.* **79**, 353–419 (2007). URL <https://link.aps.org/doi/10.1103/RevModPhys.79.353>.
- [34] Bardeen, J. Electron-phonon interactions and superconductivity. *Science* **181**, 1209–1214 (1973). URL <https://science.sciencemag.org/content/181/4106/1209>.
- [35] Nayak, C., Simon, S. H., Stern, A., Freedman, M. & Das Sarma, S. Non-abelian anyons and topological quantum computation. *Rev. Mod. Phys.* **80**, 1083–1159 (2008). URL <https://link.aps.org/doi/10.1103/RevModPhys.80.1083>.
- [36] Joynt, R. & Taillefer, L. The superconducting phases of UPT₃. *Rev. Mod. Phys.* **74**, 235–294 (2002). URL <https://link.aps.org/doi/10.1103/RevModPhys.74.235>.
- [37] Avers, K. E. *et al.* Broken time-reversal symmetry in the topological superconductor UPT₃. *Nature Physics* **16**, 531–535 (2020). URL <https://doi.org/10.1038/s41567-020-0822-z>.
- [38] Jiao, L. *et al.* Chiral superconductivity in heavy-fermion metal UTe₂. *Nature* **579**, 523–527 (2020). URL <https://doi.org/10.1038/s41586-020-2122-2>.
- [39] Zhang, P. *et al.* Observation of topological superconductivity on the surface of an iron-based superconductor. *Science* **360**, 182–186 (2018). URL <https://science.sciencemag.org/content/360/6385/182>.
- [40] Li, Y. *et al.* Electronic properties of the bulk and surface states of Fe_{1+y}Te_{1-x}Se_x. *Nature Materials* (2021). URL <https://doi.org/10.1038/s41563-021-00984-7>.
- [41] Lian, B., Liu, Z., Zhang, Y. & Wang, J. Flat chern band from twisted bilayer MnBi₂Te₄. *Phys. Rev. Lett.* **124**, 126402 (2020). URL <https://link.aps.org/doi/10.1103/PhysRevLett.124.126402>.
- [42] Kennes, D. M., Xian, L., Claassen, M. & Rubio, A. One-dimensional flat bands in twisted bilayer germanium selenide. *Nature Communications* **11**, 1124 (2020). URL <https://doi.org/10.1038/s41467-020-14947-0>.
- [43] Morales-Durán, N., Hu, N. C., Potasz, P. & MacDonal, A. H. Non-local interactions in moiré Hubbard systems. *arXiv:2108.03313* (2021). URL <https://arxiv.org/abs/2108.03313>.

- [44] Metzner, W., Salmhofer, M., Honerkamp, C., Meden, V. & Schönhammer, K. Functional renormalization group approach to correlated fermion systems. *Rev. Mod. Phys.* **84**, 299–352 (2012). URL <https://link.aps.org/doi/10.1103/RevModPhys.84.299>.
- [45] Nandkishore, R., Chern, G.-W. & Chubukov, A. V. Itinerant Half-Metal Spin-Density-Wave State on the Hexagonal Lattice. *Phys. Rev. Lett.* **108**, 227204 (2012). URL <https://link.aps.org/doi/10.1103/PhysRevLett.108.227204>.
- [46] Martin, I. & Batista, C. D. Itinerant Electron-Driven Chiral Magnetic Ordering and Spontaneous Quantum Hall Effect in Triangular Lattice Models. *Phys. Rev. Lett.* **101**, 156402 (2008). URL <https://link.aps.org/doi/10.1103/PhysRevLett.101.156402>.
- [47] Nandkishore, R., Thomale, R. & Chubukov, A. V. Superconductivity from weak repulsion in hexagonal lattice systems. *Phys. Rev. B* **89**, 144501 (2014). URL <https://link.aps.org/doi/10.1103/PhysRevB.89.144501>.
- [48] Honerkamp, C. Instabilities of interacting electrons on the triangular lattice. *Phys. Rev. B* **68**, 104510 (2003). URL <https://link.aps.org/doi/10.1103/PhysRevB.68.104510>.
- [49] Note that the number of nodes on the Fermi surface depends on the chemical potential. It is four if the Fermi surface is closer to Γ (where we do not find a superconducting instability), and eight near Van Hove energy (where we do find one).
- [50] Sigrist, M. & Ueda, K. Phenomenological theory of unconventional superconductivity. *Rev. Mod. Phys.* **63**, 239–311 (1991). URL <https://link.aps.org/doi/10.1103/RevModPhys.63.239>.
- [51] Volovik, G. E. On edge states in superconductors with time inversion symmetry breaking. *Journal of Experimental and Theoretical Physics Letters* **66**, 522–527 (1997). URL <https://doi.org/10.1134/1.567563>.
- [52] Read, N. & Green, D. Paired states of fermions in two dimensions with breaking of parity and time-reversal symmetries and the fractional quantum Hall effect. *Phys. Rev. B* **61**, 10267–10297 (2000). URL <https://link.aps.org/doi/10.1103/PhysRevB.61.10267>.
- [53] Black-Schaffer, A. M. & Honerkamp, C. Chiral d -wave superconductivity in doped graphene. *Journal of Physics: Condensed Matter* **26**, 423201 (2014). URL <https://doi.org/10.1088/0953-8984/26/42/423201>.
- [54] Senthil, T., Marston, J. B. & Fisher, M. P. A. Spin quantum Hall effect in unconventional superconductors. *Phys. Rev. B* **60**, 4245–4254 (1999). URL <https://link.aps.org/doi/10.1103/PhysRevB.60.4245>.
- [55] Horovitz, B. & Golub, A. Superconductors with broken time-reversal symmetry: Spontaneous magnetization and quantum Hall effects. *Phys. Rev. B* **68**, 214503 (2003). URL <https://link.aps.org/doi/10.1103/PhysRevB.68.214503>.
- [56] Zhou, S. & Wang, Z. Nodal $d + id$ Pairing and Topological Phases on the Triangular Lattice of $\text{Na}_x\text{CoO}_2 \cdot y\text{H}_2\text{O}$: Evidence for an Unconventional Superconducting State. *Phys. Rev. Lett.* **100**, 217002 (2008). URL <https://link.aps.org/doi/10.1103/PhysRevLett.100.217002>.
- [57] Kiesel, M. L., Platt, C., Hanke, W. & Thomale, R. Model evidence of an anisotropic chiral $d+id$ -wave pairing state for the water-intercalated $\text{Na}_x\text{CoO}_2 \cdot y\text{H}_2\text{O}$ superconductor. *Phys. Rev. Lett.* **111**, 097001 (2013). URL <https://link.aps.org/doi/10.1103/PhysRevLett.111.097001>.
- [58] Halbertal, D. *et al.* Moiré metrology of energy landscapes in van der waals heterostructures. *Nature Communications* **12**, 242 (2021). URL <https://doi.org/10.1038/s41467-020-20428-1>.
- [59] Hauck, J. B., Honerkamp, C., Achilles, S. & Kennes, D. M. Electronic instabilities in Penrose quasicrystals: Competition, coexistence, and collaboration of order. *Phys. Rev. Research* **3**, 023180 (2021). URL <https://link.aps.org/doi/10.1103/PhysRevResearch.3.023180>.
- [60] Wolf, S., Di Sante, D., Schwemmer, T., Thomale, R. & Rachel, S. Triplet superconductivity from non-local Coulomb repulsion in Sn/Si (111). *arXiv:2107.03482* (2021). URL <https://arxiv.org/abs/2107.03482>.
- [61] Black-Schaffer, A. M. Edge Properties and Majorana Fermions in the Proposed Chiral d -Wave Superconducting State of Doped Graphene. *Phys. Rev. Lett.* **109**, 197001 (2012). URL <https://link.aps.org/doi/10.1103/PhysRevLett.109.197001>.
- [62] Platt, C., Hanke, W. & Thomale, R. Functional renormalization group for multi-orbital fermi surface instabilities. *Advances in Physics* **62**, 453–562 (2013). URL <https://doi.org/10.1080/00018732.2013.862020>.
- [63] Dupuis, N. *et al.* The nonperturbative functional renormalization group and its applications. *Physics Reports* **910**, 1–114 (2021). URL <https://doi.org/10.1016/j.physrep.2021.01.001>.